Biomaterials Advances 153 (2023) 213564

Contents lists available at ScienceDirect

Biomaterials Advances

journal homepage: www.journals.elsevier.com/materials-science-and-engineering-c

The shape of our gut: Dissecting its impact on drug absorption in a 3D bioprinted intestinal model

Maria Helena Macedo [a,b,c,1], Núria Torras [d], María García-Díaz [d], Cristina Barrias [a,b,c], Bruno Sarmento [a,b,e], Elena Martínez [d,f,g,*]

[a] i3S – Instituto de Investigação e Inovação em Saúde, Rua Alfredo, Universidade do Porto, Rua Alfredo Allen 208, 4200-135 Porto, Portugal
[b] INEB – Instituto Nacional de Engenharia Biomédica, Universidade do Porto, Rua Alfredo Allen 208, 4200-135 Porto, Portugal
[c] ICBAS – Instituto de Ciências Biomédicas Abel Salazar, Universidade do Porto, Rua Jorge Viterbo Ferreira 228, 4050-313 Porto, Portugal
[d] IBEC – Institute for Bioengineering of Catalonia, BIST - The Barcelona Institute of Science and Technology, Baldiri Reixac 10-12, 08028 Barcelona, Spain
[e] CESPU – Instituto de Investigação e Formação Avançada em Ciências e Tecnologias da Saúde, Rua Central de Gandra 1317, 4585-116 Gandra, Portugal
[f] CIBER-BBN – Consorcio Centro de Investigación Biomédica en Red de Bioingeniería, Biomateriales y Nanomedicina, Avenida Monforte de Lemos 3-5, 28029 Madrid, Spain
[g] Electronics and Biomedical Engineering Department, Universitat de Barcelona, Martí I Franquès 1, 08028 Barcelona, Spain

ARTICLE INFO

Keywords:
3D bioprinting
Photopolymerization
Intestinal models
Villi
3D architecture
Intestinal absorption
Drug development

ABSTRACT

The small intestine is a complex organ with a characteristic architecture and a major site for drug and nutrient absorption. The three-dimensional (3D) topography organized in finger-like protrusions called villi increases surface area remarkably, granting a more efficient absorption process. The intestinal mucosa, where this process occurs, is a multilayered and multicell-type tissue barrier.

In vitro intestinal models are routinely used to study different physiological and pathological processes in the gut, including compound absorption. Still, standard models are typically two-dimensional (2D) and represent only the epithelial barrier, lacking the cues offered by the 3D architecture and the stromal components present *in vivo*, often leading to inaccurate results. In this work, we studied the impact of the 3D architecture of the gut on drug transport using a bioprinted 3D model of the intestinal mucosa containing both the epithelial and the stromal compartments. Human intestinal fibroblasts were embedded in a previously optimized hydrogel bioink, and enterocytes and goblet cells were seeded on top to mimic the intestinal mucosa. The embedded fibroblasts thrived inside the hydrogel, remodeling the surrounding extracellular matrix. The epithelial cells fully covered the hydrogel scaffolds and formed a uniform cell layer with barrier properties close to *in vivo*. In particular, the villus-like model revealed overall increased permeability compared to a flat counterpart composed by the same hydrogel and cells. In addition, the efflux activity of the P-glycoprotein (P-gp) transporter was significantly reduced in the villus-like scaffold compared to a flat model, and the genetic expression of other drugs transporters was, in general, more relevant in the villus-like model. Globally, this study corroborates that the presence of the 3D architecture promotes a more physiological differentiation of the epithelial barrier, providing more accurate data on drug absorbance measurements.

1. Introduction

The small intestine is the major site of nutrient and drug absorption in the body. It is a complex organ with a characteristic three-dimensional (3D) architecture and cell composition. The intestinal tissue is organized in finger-like protrusions called villi and invaginations called crypts. These greatly increase the tissue surface area and, therefore, the volume and residence time of fluids, enhancing intestinal absorption [1–3]. For a molecule to reach systemic circulation, it needs to cross the intestinal epithelium and the lamina propria, both forming the intestinal mucosa, to enter the bloodstream through the blood capillaries [4]. The intestinal epithelium is composed by absorptive cells –

* Corresponding author at: IBEC – Institute for Bioengineering of Catalonia, BIST - The Barcelona Institute of Science and Technology, Baldiri Reixac 10-12, 08028 Barcelona, Spain.
E-mail address: emartinez@ibecbarcelona.eu (E. Martínez).
[1] Present address: INL - International Iberian Nanotechnology Laboratory, Avenida Mestre José Veiga, 4715-330 Braga, Portugal.

https://doi.org/10.1016/j.bioadv.2023.213564
Received 11 January 2023; Received in revised form 13 June 2023; Accepted 18 July 2023
Available online 20 July 2023

the enterocytes, goblet cells, enteroendocrine cells, Paneth cells, tuft cells, and microfold cells [4–6]. The lamina propria, in its turn, contains fibroblasts, myofibroblasts, mesenchymal stem cells, endothelial, and immune cells embedded in the extracellular matrix (ECM) [7,8]. The lamina propria and its interactions with the intestinal epithelium, referred as epithelial-mesenchymal crosstalk, are important to maintain the integrity of the intestinal mucosa [9,10]. This crosstalk shapes the architecture of the small intestine, as well as its functions, being essential to maintain cell polarity, behavior and differentiation during intestinal development [11–13]. These interactions also play a role in cell proliferation, migration and apoptosis, contributing to overall tissue homeostasis [14].

Although major developments and breakthroughs have been made in getting *in vitro* models of the intestine [15–20], neither the stromal compartment nor the 3D architecture are usually present in the standard assays used to test drug absorption, study cellular behavior or model diseases. The gold standard model for drug permeability assays is composed of a flat polarized monolayer of enterocyte-like Caco-2 cells. It only represents one compartment of the intestinal mucosa - the epithelium - and one cell type - the enterocytes -, and misses the characteristic 3D topographical features of the native tissue [21]. It also presents drawbacks regarding functional aspects. Compared with the human intestine, the Caco-2 model has different expression levels of drug transporters and forms a tighter barrier, which can both lead to low accuracy when predicting drug intestinal permeability [22]. On the other hand, the 3D architecture generates oxygen and molecular gradients that dictate the distribution of the different cell types along the crypt-villus axis, being essential for cell renewal and tissue homeostasis [23–25]. Thus, new *in vitro* models that better represent the epithelial-stromal crosstalk together with the architecture of the human small intestine are needed to help bridge the *in vitro/in vivo* gap.

The presence of the stromal compartment in intestinal *in vitro* 3D models triggers a more physiological behavior of epithelial cells [10,27]. We have demonstrated this epithelial-stromal crosstalk in two different approaches that recreate the stromal compartment using fibroblast-laden hydrogels. First, we used a hydrogel *co*-network of poly (ethylene glycol) diacrylate (PEGDA) and gelatin methacryloil (GelMA) embedding the stromal fibroblasts, and seeded Caco-2 cells on top to form the epithelial barrier. The presence of the stromal cells promoted the epithelial barrier formation and accelerated barrier integrity recovery upon a temporary disruption of the epithelial tight junctions [10]. Increasing the cellular diversity, we developed an innovative model composed by an epithelium of enterocytes and goblet cells on top of a collagen layer laden with human intestinal fibroblasts (HIFs) and an endothelial layer underneath [27]. The stromal-epithelial interactions that closely resembled the *in vivo* environment led to a barrier tightness and permeability values more similar to the human intestine, and promoted a physiologically relevant expression of most drug transporters [27].

On the other hand, it has been demonstrated the effect of the characteristic microstructured topography of the small intestine on the epithelial barrier [3,26,28]. The villi, finger-like protrusions of 0.2–1 mm in height and 100–200 μm in diameter, have a well-defined topography and curvature that provides environmental cues to the epithelial cells growing on top [26,29,30]. However, only few works have mimicked the epithelial-stromal crosstalk in 3D microstructured intestinal models, most of them using 3D extrusion bioprinting [15–17]. Kim & Kim used a dual-cell extrusion system to obtain a 3D intestinal villi model containing an epithelial layer and a blood capillary structure using two collagen-based bioinks laden with Caco-2 cells and endothelial cells [15,16]. Madden et al. also used extrusion-based bioprinting to obtain a flat model of the small intestine using primary human enterocytes and myofibroblasts, using the thermo-responsive Novogel® bioink [17]. None of these models addressed the changes in the drug cellular transporters derived from their improved features, a key property for drug absorption.

In here, we have developed a physiologically relevant *in vitro* model of the small intestine, with both the 3D villus-like architecture and the stromal compartment by using digital light projection stereolithography (DLP-SLA) bioprinting method recently developed in our lab [31]. We optimized the bioink containing the cell-adhesive polymer GelMA, the synthetic polymer PEGDA, the photoinitiator LAP, and the photoabsorber tartrazine [31]. This bioink provided structural support for the bioprinting of the high aspect-ratio villi structures mimicking the small intestine architecture while maintaining a cell-friendly matrix for the encapsulated stromal fibroblasts. This stromal compartment supported the growth of the epithelial cell barrier, recapitulating the anatomical subepithelial location of the intestinal fibroblasts. Using the 3D model, we demonstrated the effect of the intestinal topography on cell differentiation, expression of drug transporters and permeability outcomes, and the relevance of including the 3D architecture and the stromal compartment for obtaining a model of the intestinal mucosa with *in vivo*-like properties.

2. Materials and methods

2.1. Cell culture

Caco-2 C2BBe1 (described as Caco-2 cells in the manuscript) were purchased from American type culture collection (ATCC) and mucus producing HT29-MTX cells were kindly provided by Dr. T. Lesuffleur (INSERM U178, Villejuif, France). Caco-2 (passages 53 to 57) and HT29-MTX cell lines (passages 37 to 50) were grown in Dulbecco's modified Eagle's medium (DMEM) with 4.5 g/L glucose and Ultraglutamine™ (Gibco), supplemented with 1 % Penicillin/Streptomycin 100× (Biowest) and 10 % Fetal Bovine Serum (FBS) (Biochrom), named as complete DMEM.

Human intestinal fibroblasts (HIF) primary cells (passage 5–6) were obtained from ScienCell and were cultured in Fibroblast medium (FM) supplemented with 2 % FBS, 1 % of Fibroblast Growth Supplement (FGS) and 1 % of penicillin/streptomycin solution (all from ScienCell).

All cells were grown separately in T75 and T175 tissue culture flasks (Nunc) and maintained in an incubator Series II Water Jacket CO_2 incubator (Thermo Scientific) at 37 °C and 5 % CO_2, in a water saturated atmosphere.

2.2. Fabrication of the bioprinted models of the intestinal mucosa

A low-cost digital light processing stereolithography (DLP-SLA) system based on a commercially available SOLUS 3D printer (Junction3D) was employed for the fabrication of fibroblast-laden hydrogels with and without (called flat) villus-like microstructures. For the printing, a bioink composed of 5 % (w/v) GelMA, 3 % (w/v) PEGDA, 0.4 % (w/v) lithium phenyl-2,4,6-trimethylbenzoylphosphinate (LAP) and 0.025 % (w/v) tartrazine dissolved in Hank's Balanced Salt Solution (HBSS) supplemented with 1 % penicillin/streptomycin was mixed with the target amount of fibroblast and crosslinked by using visible-light photopolymerization. The bioink was placed in a customized cuvette at 37 °C and the villus-like microstructures were printed layer-by-layer by projecting series of black and white patterns from a CAD design. A full high-definition 1080p resolution projector (Vivitek) with optical power density applied for printing of 12.3 mW/cm^2 within the spectral range from 320 to 640 nm wavelength was employed. To avoid cell damage due to infrared (IR) radiation exposure, a KG3 SCHOTT short pass heat protection filter (ITOS, Edmund Optics) was added. A detailed explanation of the printing device and procedure can be found elsewhere [31] and a schematic representation in Supplementary Fig. S1. CAD designs featuring (i) villus-like structures of 750 μm in height and 300 μm in diameter spaced 750 μm on top of a disc-like base of 250 μm, or (ii) flat disc-like hydrogels of 300 μm in height (both designs were 6.5 mm in diameter) were printed using previously optimized printing parameters [31]: 13 μm of layer thickness and 5 s of exposure time. To ease the

handling of the printed hydrogels, silanized polyethylene terephthalate (PET) Tracketch® membranes with 10 mm in diameter (SABEU) were attached to the bottom part of the printing support as printing substrates. Once printed, the samples were rinsed in warm phosphate buffered saline (PBS) containing 1 % of penicillin/streptomycin and assembled in Transwell® inserts by means of two pressure sensitive adhesive (PSA) rings as described in [10].

2.3. HIF viability inside the bioprinted hydrogels

To determine the viability of the fibroblasts inside the bioprinted scaffolds along the time in culture, a live/dead (L/D) assay was performed at different timepoints (7, 14 and 21 days). Flat hydrogels with two different HIF initial densities (2.5 and 5 × 10^6 cells/mL) were produced as described in Section 2.2, and kept in DMEM supplemented with Normocin (1:500, Ibian Technologies) for 21 days. At selected time points, the assay was performed using the calcein-AM/ethidium homodimer L/D kit (Invitrogen). Samples were washed three times with PBS for 5 min each, after which the L/D solution was added, and samples were incubated at 37 °C in the dark for 20–30 min. Then, samples were washed again three times for 5 min and mounted for microscope visualization. A confocal laser scanning microscope (LSM 800, Zeiss) was used, and ImageJ software version 2.1.0/1.53c (http://rsb.info.nih.gov/ij, NIH) was employed for image processing.

2.4. HIF morphology and extracellular matrix secretion inside the hydrogels

After 21 days in culture, the HIF-laden hydrogels were washed (all washing steps were performed thrice with PBS for 5 min in shaking conditions) and fixed using 500 μL of formalin solution, neutral buffered, 10 % (Sigma) for 30 min under shaking conditions at room temperature. After fixation, the samples were washed and permeabilized using a solution of 0.5 % Triton X-100 (Sigma) in PBS and incubated for 2 h at 4 °C in shaking conditions. After permeabilization, samples were washed again and then a blocking step was performed using a blocking solution (BS) containing 1 % bovine serum albumin (BSA) (Life technologies), 3 % donkey serum (Merck) and 0.3 % Triton X-100 in PBS, for 2 h at 4 °C in shaking conditions. Samples were then washed and incubated with the primary antibodies' solutions. Mouse anti-human vimentin (1:50) (sc-6260, Santa Cruz Biotechnolgy) + rabbit anti-human fibronectin (1:100) (F3648, Sigma) or mouse anti-human alpha smooth muscle actin (alpha-SMA) (1:200) (ab7817, Abcam) + goat anti-human collagen type IV (1:250) (134001, Biorad) were diluted in the primary working buffer (PWB) containing 0.1 % BSA, 0.3 % donkey serum and 0.2 % Triton X-100 in PBS and incubated with the samples overnight (ON), at 4 °C in shaking conditions. Then, samples were washed once again and were incubated in the secondary working buffer (SWB) containing 0.1 % BSA and 0.3 % donkey serum in PBS and the secondary antibodies donkey anti-mouse IgG (H + L) highly cross-adsorbed Alexa Fluor 488 (1:500) (Invitrogen A-21202), donkey anti-rabbit IgG (H + L) highly cross-adsorbed Alexa Fluor 568 (1:500) (Invitrogen A-10042) and donkey anti-goat IgG (H + L) cross-adsorbed Alexa Fluor 647 (1:500) (Invitrogen A-21447), accordingly to the primary antibodies' combinations. DAPI (1:1000) (Fisher Scientific) and Rhodamine Phalloidin (1:140) (Cytoskeleton) were incubated together with the secondary antibodies for 2 h at 4 °C under shaking conditions, protected from light. After incubation, samples were washed one last time and kept in PBS until visualization using a confocal laser scanning microscope LSM 800 (Zeiss). ImageJ software was employed for image processing.

2.5. Epithelial cell seeding

The day after bioprinting, epithelial cells were seeded on top of the HIF-laden hydrogels with and without villus-like microstructures (thereafter named as "villi" and "flat"). Caco-2 and HT29-MTX cells (7.5 × 10^5 cells/cm^2 at a 9:1 ratio, respectively) in 0.2 mL of DMEM complete supplemented with Normocin were seeded on top of the samples. The cultures were incubated at 37 °C, 5 % CO_2 in a water saturated atmosphere and were maintained for 21 days, changing the medium every 2–3 days. Before changing the medium, transepithelial electrical resistance (TEER) was measured using EVOM^3 and EndOhm-6G (World Precision Instruments). Pictures were taken along the time in culture to assess cell growth and epithelial layer formation on top of the HIF-laden hydrogels using an Eclipse Ts2 microscope (Nikon).

2.6. Quantification of intestinal differentiation markers

The alkaline phosphatase (ALP) activity was quantified in the bioprinted intestinal models using a colorimetric alkaline phosphatase assay kit (ab83369, Abcam), as described by the manufacturer. Briefly, medium from the apical side of the models was retrieved at different timepoints (7, 14 and 21 days) and ALP activity was measured immediately. For this, medium samples from the cultures, sample background control (culture medium) and *p*-nitrophenyl phosphate (pNPP) standards were added to a 96-well plate (ThermoScientific). 20 μL of stop solution were added to the sample background control wells. Then, 50 μL of 5 mM pNPP were added to each well containing the samples and the sample background control. Finally, 10 μL of ALP enzyme were added to each standard. The plate was incubated for 60 min at room temperature and protected from light. Reaction stopped by adding 20 μL of Stop Solution to the samples and standard wells. The plate was carefully shaken, and the absorbance was read at 405 nm using an Infinite M200 PRO multimode microplate reader (Tecan).

The genetic expression of the intestinal markers Intestine Specific Homeobox (ISX), Sucrase Isomaltase (SI) and Villin1 (VIL1) was assessed using Real Time quantitative Polymerase Chain Reaction (RT-qPCR). At day 21 in culture, RNA extraction of both flat and villi models was performed using a Quick-RNA MiniPrep kit (Zymo Research), according to manufacturer's instructions. Briefly, cells were lysed by removing the culture medium from the inserts, adding RNA lysis buffer directly on top of the hydrogels and pipetting up and down to completely dissolve it. The solution was centrifuged (all centrifugation steps were performed at 13,000*g* for 30 s, otherwise noted) and the supernatant was transferred to a Spin-Away filter in a collection tube and centrifuged again. The flow through was used for RNA purification. For this, 96 % ethanol was added to the samples in a 1:1 proportion and thoroughly mixed. The resulting solution was transferred to a ZymoSpin IIICG column in a collection tube and centrifuged. A treatment with DNAse I was then performed to remove genomic DNA. The column was firstly washed with RNA wash buffer, followed by centrifugation and incubation with DNAse I reaction mix for 30 min at room temperature. Samples were once again centrifuged and RNA Prep Buffer was added, followed by another centrifugation. To ensure complete washing of the samples, RNA wash buffer was added to the samples twice and in the last wash the centrifugation was performed for 1 min to ensure complete removal of the buffer. The columns were carefully transferred into RNAse-free tubes and 50 μL of DNAse/RNAse-Free water were added directly to the column and centrifuged. The eluted RNA was stored at −80 °C until further use.

The quality and concentration of the sample's RNA was evaluated in an automated electrophoresis station (Experion Automated Electrophoresis System, Bio-rad) using Experion RNA StdSens Kit (700–7105, Bio-rad) according to manufacturer's instructions, using 1 μL of RNA in a quantification range of 5–500 ng/μL of each purified total RNA sample.

Reverse Transcriptase (RT) was performed to obtain cDNA from the RNA samples. For this, an iScript cDNA Synthesis Kit (1708891, Bio-rad) was used following manufacturer's instructions. Briefly, RNA template was mixed with 5× iScript Reaction Mix, iScript Reverse Transcriptase and Nuclease free water. Samples were placed in a thermal cycler (T100 Thermal Cycler, Bio-rad) and the protocol was initiated, which consisted

in a priming step of 5 min at 25 °C followed by a reverse transcription step for 20 min at 46 °C and an inactivation step for 1 min at 95 °C.

qPCR was performed using the obtained cDNA. A primePCR plate (Biorad) customized with the genes of interest and the housekeeping genes Glyceraldehyde 3-phosphate dehydrogenase (GAPDH) and Actin Beta (ACTB) was used (Bio-rad). First, 1 μL of RT control template was added to each 20 μL of cDNA synthesis reaction. The master mixes were prepared adding iTaq Universal SYBR Green Supermix (Bio-rad), cDNA template and Nuclease Free Water according to manufacturer's instructions. The protocol was run using a real time PCR instrument (CFX96 Touch Real-Time PCR Detection System, Bio-rad), according to the prime PCR plate protocol, which consisted in an activation step at 95 °C for 2 min, followed by 40 cycles of a denaturation step for 5 s also at 95 °C and an annealing/extension step at 60 °C for 30 s The melt curve was performed between 65 °C and 95 °C in 0.5 °C increments for 5 s/step.

2.7. Quantification of genetic expression of intestinal drug transporters

The genetic expression of different drug transporters [ABCB1 - P-glycoprotein (P-gp); ABCC1 - Multidrug Resistance Protein 1 (MRP1); ABCC2 - Multidrug Resistance Protein 2 (MRP2); ABCG2 – Breast Cancer Resistance Protein (BCRP); SLC15A1 – Peptide Transporter 1 (PEPT1); SLC16A1 – Monocarboxylate Transporter 1 (MCT1); SLC22A1 – Organic Cationic Transporter 1 (OCT1)] was assessed using Reverse Transcriptase Real Time quantitative Polymerase Chain Reaction (RT-qPCR), exactly as described in the previous section.

2.8. Immunostaining

To confirm the integrity of the epithelial layer and to assess the expression of different proteins in the villi model, immunocytochemistry was performed. We assessed the expression of Zonna Occludens 1 (ZO-1), a tight junction protein with β-catenin, a protein that is involved in cellular adhesion. The presence of fibronectin and collagen type IV in the hydrogels was also assessed.

To preserve the morphology of the villus-like hydrogels, samples were first embedded in a PEGDA solution based on a protocol developed by Altay et al. [26]. Briefly, after a fixation step with 10 % formalin for 30 min under shaking conditions at room temperature, samples were submerged in a pre-polymer solution containing 10 % w/v PEGDA 575 kDa (Sigma) and 1 % w/v Irgacure D-2959 photoinitiator (Sigma) in PBS and kept ON at 4 °C. Samples were then placed in polydimethylsiloxane (PDMS) round pools of 12 mm diameter and 2 mm thickness attached to a plastic support, and PEGDA 575 kDa pre-polymer solution was used to fill the pools. Constructs were irradiated using ultraviolet (UV) light at 365 nm in a MJB4 mask aligner (SÜSS MicroTech). First, a 40 s at 25 mW/cm^2 of power density exposure was performed to form a support base to keep the constructs in place. Samples were irradiated twice for 100 s, first from the top and then from the bottom, to ensure the formation of a homogeneous block surrounding them. After UV exposure, unreacted polymer and photoinitiator solutions were washed out using PBS. Then, samples were incubated ON with 30 % sucrose (Sigma) and then embedded in optimal cutting temperature (OCT) compound (Sakura® Finetek). Samples were cut to obtain histological cross-sections of around 7 μm thickness, attached onto glass slides, air dried and stored at −20 °C until use.

For immunostaining, slides were carefully washed with PBS at room temperature to dissolve the OCT. A solution containing 0.5 % Triton X-100 in PBS was used for cellular permeabilization. Slides were incubated with this solution in a humidified chamber for 1 h at 4 °C under gentle shaking. After the permeabilization, samples were washed again with PBS and a blocking step was performed to avoid unspecific binding of the antibodies. The BS was added to the samples in the humified chamber and kept for 2 h at 4 °C under gentle shaking. Samples were washed and incubated with the primary antibodies' [rabbit anti-human fibronectin (1:100) (Sigma F3648) or goat anti-human collagen type IV (1:250) (134001, Biorad)] diluted in PWB in the humidified chamber at 4 °C under gentle shaking ON. In case of rabbit anti-human β-catenin (1:100) (ab2365, Abcam) or goat anti-human ZO-1 (1:100) (Abcam ab99462) primary antibodies, an antigen retrieval treatment was performed prior sample permeabilization to enhance the signal: briefly, samples were boiled for 10 min after unfreezing in citrate buffer solution (10 mM citrate and 0.05 % of Tween20 in MilliQ water, previously adjusting the pH at 6), controlling bubble formation. Then, the staining procedure continued as for the other markers.

The next day samples were washed with PBS and incubated with the secondary antibodies diluted in SWB. Secondary antibodies used were donkey anti-rabbit IgG (H + L) highly cross-adsorbed Alexa Fluor 647 and 568 (A-31573 and A-10042, Invitrogen), donkey anti-mouse IgG (H + L) highly cross-adsorbed Alexa Fluor 488 (A-21202, Invitrogen) and donkey anti-goat IgG (H + L) highly cross-adsorbed Alexa Fluor 647 (1:500) (A-21447, Invitrogen), accordingly to the primary antibodies' combinations. DAPI (1:100) (Fisher Scientific) and Rhodamine Phalloidin (1:140) (Cytoskeleton PHDR1) were incubated together with the secondary antibodies for 2 h at 4 °C under shaking conditions, protected from light. Finally, samples were washed with PBS and mounted using Fluoromount-G (SouthernBiotech) and kept at 4 °C, protected from light until visualization using a confocal laser scanning microscope LSM 800 (Zeiss). ImageJ software was employed for image processing.

2.9. Quantification of the activity of P-glycoprotein (P-gp)

The activity of the P-gp transporter was assessed with a transport assay using Rho 123 (Enzo Life Sciences) - a P-gp substrate. The transport was determined in both apical to basolateral and basolateral to apical directions.

After 21 days of culture, medium was removed from both sides of the Transwell® inserts and samples were washed two times with pre-warmed HBSS (Gibco). After washing, 0.2 mL and 0.6 mL of HBSS were placed on the apical and basolateral sides of the inserts, respectively. Samples were incubated at 37 °C, 5 % CO_2 and 100 rpm for 30 min in a CO_2 Resistant Shaker (Thermo Scientific). After the 30 min, samples were placed on the apical or basolateral side (0.2 or 0.6 mL of 5 μg/mL of Rho 123, respectively) and were incubated for 4 h at 37 °C and 100 rpm. By the end, a sample of 100 μL was retrieved from the apical and basolateral side of each Transwell®. The amount of Rho 123 in the samples was measured using an Infinite M200 PRO multimode microplate reader (Tecan) at excitation/emission wavelengths of 507/529.

The permeability results were expressed in terms of apparent permeability (P_{app}), that was calculated using Eq. (1).

$$P_{app} = \frac{\Delta Q}{A \times C_0 \times \Delta t}, \quad (1)$$

where ΔQ is the amount of compound detected in the receiver compartment (mg), A is the surface area of the insert (cm^2), C_0 is the initial concentration in the donor compartment (mg/mL) and Δt is the time of the experiment (s).

2.10. Permeability assays

Permeability assays were performed with three model drugs: colchicine, atenolol, and metoprolol (all from Merck), which have low, moderate, and high intrinsic permeability, respectively.

The methodology followed for the assays has been described elsewhere [27]. Briefly, culture medium was removed and cultures were washed twice with pre-warmed HBSS. Then, 0.2 and 0.6 mL of HBSS were placed on the apical and basolateral compartments of the Transwells®, respectively, and the plate was incubated for 30 min at 37 °C, 5 % CO_2 and 100 rpm in the shaker. HBSS on the apical side was then replaced for 0.2 mL of the model drug solutions (100 μM of colchicine or

metoprolol or 200 μM of atenolol in HBSS). At pre-determined time-points (60, 120, 180 and 240 min), a sample of 50 μL was taken from the basolateral compartment and replaced by the same volume of HBSS. Drugs were quantified by High Performance Liquid Chromatography (HPLC) using an Ultra-Fast Liquid Chromatograph (UFLC) Prominence System equipped with two Pumps LC-20AD, a column oven CTO-20AC, and autosampler SIL-20AC, a System Controller CBM-20A, a degasser DGU-20A5, a RF-10Axl fluorescence detector coupled to the LC System and a LC Solution, Version 1.24 SP1 (Shimadzu). Detailed methods are described in Table S1 of Supporting information.

The permeability results are expressed in percentage of permeated amount and apparent permeability (P_{app}), that was calculated using Eq. (1).

2.11. Statistical analysis

Statistical analysis was performed using the software GraphPad Prism 8.0 (GraphPad Software Inc.). All results are represented as mean ± standard error deviation (SEM) or mean ± standard deviation (SD) or mean ± upper/lower limits. Statistical differences were calculated using 2-way analysis of variance (ANOVA) multiple comparisons test and unpaired *t*-test. The level of significance was set at probabilities of $*p < 0.05$, $**p < 0.01$, $*** < 0.001$, $****p < 0.0001$.

3. Results and discussion

3.1. Characterization of the stromal compartment of the bioprinted model of the intestinal mucosa

We evaluated the intestinal fibroblasts' viability, morphology, and ability to produce and secrete ECM components when embedded in the bioprinted GelMA-PEGDA hydrogels. To optimize the amount of stromal cells (HIF) embedded, we mixed the bioink with two different concentrations of cells (2.5 and 5 × 10^6 cells/mL) and bioprinted both flat 3D and villus-like models using the printing apparatus and conditions optimized previously [31]. Briefly, cell-containing hydrogel samples were fabricated by using a customized digital light processing (DLP) stereolithographic (SLA) 3D printing system using visible light (Fig. S1). To form the 3D printed design, series of focused white and black patterns from a CAD model were projected onto the photocrosslinkable GelMA-PEGDA prepolymer solution contained in a small cuvette (volume up to 2 mL) with a transparent bottom window, forming the 3D structures in the vertical direction onto a movable printing support, in a layer by layer fashion (Figs. 1 and S1B). To ease their later manipulation and handling, samples were printed on top of silanized 10 mm diameter PET membranes as printing support. Once the printing process was finished, samples were transferred to Transwell® inserts and kept in standard culture conditions to assess cell viability at different time points.

We found similar cell survival rates in both concentrations of encapsulated cells, with a viability close to 100 % at all time points, which is key for the establishment of the model (Fig. 2a). Within the first days in culture, the fibroblasts started to acquire their characteristic

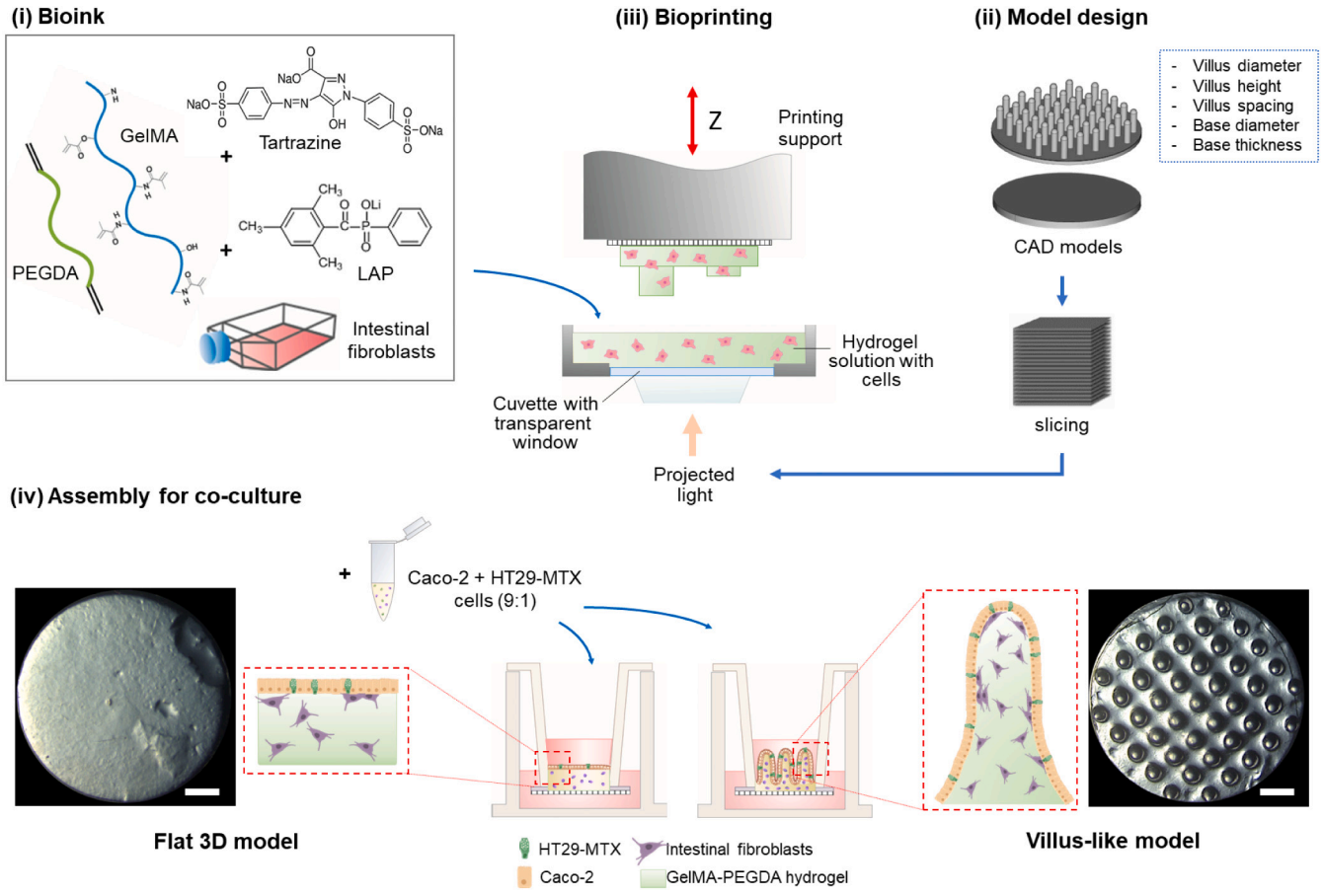

Fig. 1. Schematics of the fabrication of the 3D printed co-culture models and the main elements and steps involved: (i) the bioink preparation, (ii) the design of the models, (iii) the bioprinting process with the selection of the proper printing parameters, and (iv) the assembly of the resulting prints into Transwell® inserts for the co-culture experiments. The very same steps are required for printing both models: the flat (bottom left) and the villus-like one (bottom right). Bright field pictures show top views of the bioprinted scaffolds 3 days post HIFs encapsulation, after Transwell® assembly. Scale bars = 1 mm.

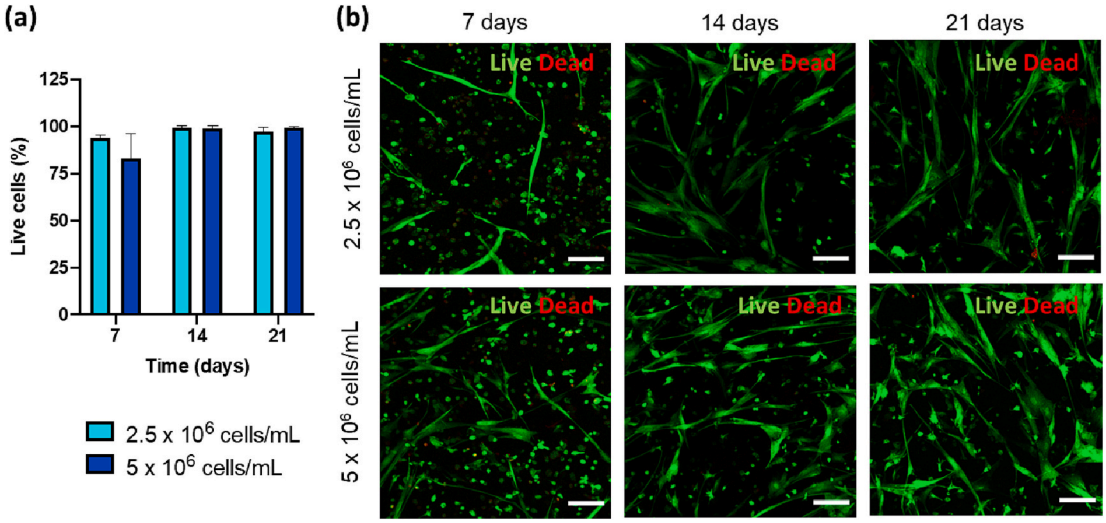

Fig. 2. Live/Dead assay performed on the HIF-laden hydrogels with two different initial cell densities. (a) Percentage of live cells and (b) maximum intensity projection (Z range 250–300 μm) of the hydrogels showing the live and dead fibroblasts (Scale bar = 100 μm).

elongated shape, showing the ability to attach and expand into the hydrogel matrix (Fig. 2b). Along the time, the number of cells showing a stretched morphology, predominantly located at the top of the sample, increased. Overall, the data on cell viability and morphology demonstrated that the bioprinting process and the bioink properties where sufficiently cell-friendly.

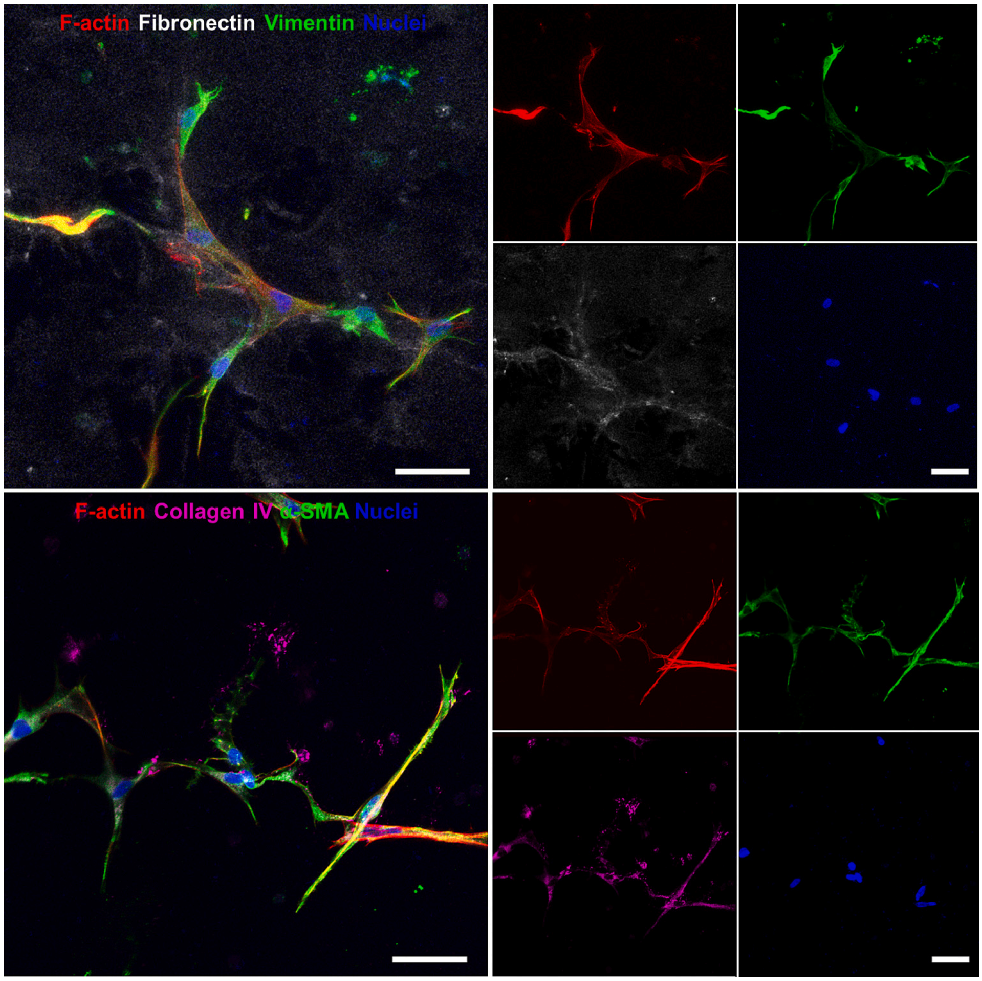

Fig. 3. Fibronectin (gray), vimentin (green), alpha-SMA (green) and collagen type IV (magenta) secretion by HIFs embedded in hydrogels (2.5 × 10^6 cells/mL) after 21 days in culture. Merged (left) and single channels (right). Fibroblasts presented an elongated shape and were able to produce and secrete ECM proteins into the hydrogel. Pictures depict a maximum intensity projection (z range 250–300 μm) (Scale bar = 50 μm).

We also analyzed the expression of several cellular and ECM proteins by immunocytochemistry. After 21 days in culture, the embedded cells expressed both vimentin and α-SMA, which indicates that they acquired a contractile phenotype, an important feature of these cells (Figs. 3 and S2) [32]. Moreover, HIFs secreted their own ECM components when entrapped inside the hydrogel, remodeling the surrounding matrix. This is shown by the presence of fibronectin and collagen type IV (Figs. 3 and S2). The ability to secrete and assemble endogenous ECM is crucial for the survival and migration of the embedded cells and to support the epithelial layer, since cell-matrix interactions play a key role in epithelial polarization, organization, and cohesiveness [9,33].

Since cellular viability and morphology was similar, and cells were able to secrete ECM proteins in both conditions, we selected the cell embedding density of 2.5×10^6 cells/mL for the follow-up studies.

3.2. Characterization of the epithelial layer on the bioprinted model of the intestinal mucosa

After optimizing the stromal compartment, we seeded Caco-2 and HT29-MTX cells on top of HIF-laden bioprinted hydrogels with (villi) and without (flat) 3D morphology and studied the cell differentiation and the barrier integrity of the epithelial monolayer formed (Fig. 4). At day 1, cells were mostly arranged into clusters, and in the villi model they only covered the base and the tip of the villi. Along the time in culture, cells proliferated and eventually covered all the surface of the scaffolds, forming a complete monolayer (Fig. 4a). The epithelial layers showcased a well polarized morphology with accumulation of F-actin at their apical sides (Fig. 4b). The villus-like microstructures were fully covered, and in some regions, cells appeared forming multilayers. Although other authors observed a similar behavior in studies using the same cell types to develop intestinal models [34–38], this effect can be also the result from the histological processing of the soft and complex microstructured samples that might not render perfectly cross-sectioned cuts.

In terms of barrier integrity, TEER values (Fig. 4d) were close to 100 Ω.cm^2 for the flat configuration. These values were notably lower, and thus more physiological, than what is normally observed in the 2D standard models [37], suggesting that the stromal compartment contributed to a more accurate representation of the epithelial barrier. These TEER values were even lower in the case of the villus-like model, around 30 Ω.cm^2, which is very close to the *in vivo* values for the rat ileum-jejunum and human jejunum (reported to be about 30 Ω.cm^2) [39,40]. Notably, a decrease in the TEER values of 3D cultures was previously observed in different works and is considered a key advantage of these models [10,27,37,41].

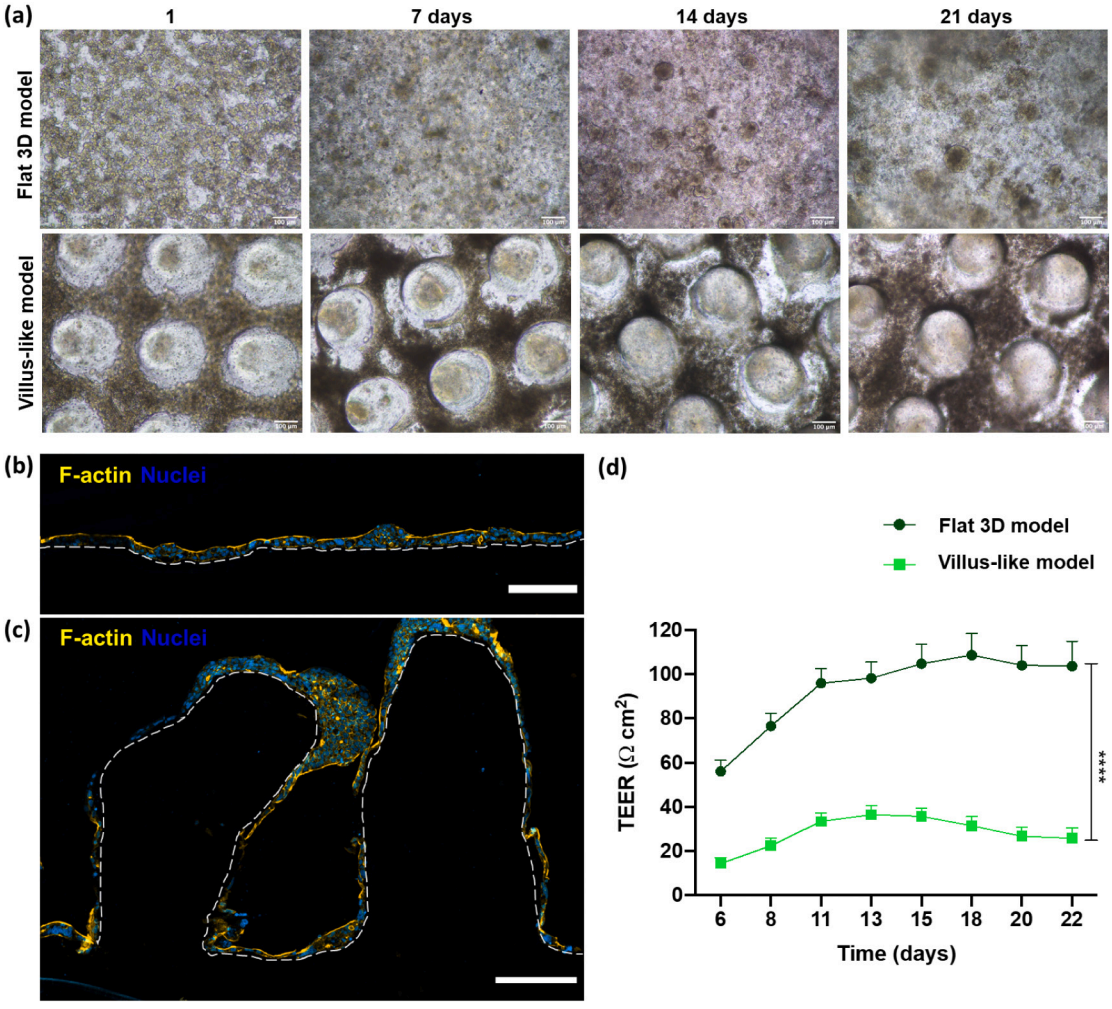

Fig. 4. Epithelial layer formation of top of the HIF-laden bioprinted hydrogels. (a) Top view of the epithelial cells on top of flat and villi scaffolds at different timepoints (1, 7, 14 and 21 days) and monolayer visualization by staining of F-actin and nuclei in transversal cuts of (b) flat and (c) villi scaffolds after 21 days in culture. Dashed lines define the hydrogel boundaries. (d) TEER values along the 21 days in culture, where results are the average of 18 samples and bars represent the standard error of the mean (SEM). Statistical difference $p < 0.0001$ are denoted by (****).

3.3. Quantification of intestinal differentiation markers

ALP is exclusively expressed by differentiated enterocytes [42,43]. We measured ALP activity in the flat and villi models to evaluate the effect of the scaffold architecture in enterocyte differentiation (Fig. 5a). In general, despite being only statistically significantly at day 7, the ALP activity was slightly higher in the villi scaffolds.

We then further determined the genetic expression of ISX, SI and VIL1 after 21 days in culture (Fig. 5b) [44–46]. ISX is a transcription factor that shows intestine-specific expression, SI is a specific gene of the enterocyte lineage, and VIL1 is expressed by mature epithelial cells [45–47]. The expression of these genes impacts intestinal permeability: ISX is involved in intestinal lipid absorption [48]; SI is the most abundant intestinal disaccharidase, so abnormal gene expression may reflect on altered absorption of carbohydrates [27,49]; and Villin is an actin-binding protein that plays a role on the organization and stabilization of the intestinal brush border [47].

Herein, we found a non-statistically significant expression of these markers in both configurations. The slightly lower expression of ISX in the villi model may be related with a higher number of HT29-MTX cells in these cultures, as it has previously been reported [27]. Overall, these results, combined to what was observed for ALP activity, suggest that the 3D architecture does not have a remarkable impact in the expression of intestinal differentiation markers with the cell models employed.

3.4. Gene expression of drug transporters

Drug transporters play a major role in the absorption of many compounds and have a great influence in drug absorption by impacting the pharmacokinetics and pharmacodynamics of drugs, influencing drugs disposition and interactions [50,51].

We compared the genetic expression of different intestinal transporters involved in the influx and efflux of compounds in the 3D bioprinted models of intestinal mucosa as compared to the conventional 2D co-culture model composed by Caco-2 and HT29-MTX, from our previous study (Fig. 6) [27]. When looking at the expression of the influx transporters PEPT1 (SLC15A1), OCT1 (SLC22A1) and MCT1 (SLC16A1), our 3D models showed a significant decrease compared with the 2D model. Comparing the two 3D bioprinted models (villi and flat), PEPT1 (SLC15A1) and OCT1 (SLC22A1) were significantly less expressed when cells were cultured in a villus-like topography. PEPT1 is expressed at the apical side of enterocytes and plays a role in the absorption processes [52,53]. When looking at the spatial expression of this transporter in the human intestine, literature data indicates a high expression in the duodenum and negligible expression in the jejunum and ileum [54]. In Caco-2 cells, there are reports showing lower expression of PEPT1 compared to the human small intestine, however its expression greatly varies depending on the cell origin or culture conditions [52,53,55]. The lower expression of this transporter we found in the bioprinted villi configuration suggests that this model might better mimic the intestinal drug transporters of the jejunum and ileum. In contrast, the flat model may be more suitable to test the permeability of drugs that are substrates of PEPT1 in the duodenum, where the *in vivo* expression is found to be high [54]. OCT1 (SLC22A1), on the other hand, is expressed at the basolateral side of enterocytes and reportedly overexpressed in standard Caco-2 models [50,56,57]. In our bioprinted 3D models this transporter is significantly less expressed compared to the 2D co-culture model, especially in the villi configuration, leading to a more physiological expression. MCT1 (SLC16A1) is another influx transporter that is overexpressed in 2D Caco-2 models [56]. Again, the lower expression in the bioprinted models, especially in the villi configuration, suggest that they represent better the intestinal barrier than conventional 2D models.

We also studied the expression of the efflux transporters P-gp (ABCB1), MRP1 (ABCC1), MRP2 (ABCC2) and BCRP (ABCG2) in the 3D bioprinted models. P-gp and MRP2 are localized at the apical surface of intestinal enterocytes, acting as an important barrier to drug absorption by being able to pump compounds back into the lumen [50,58]. A myriad of compounds are substrates of these transporters and their reported overexpression in *in vitro* 2D standard models can lead to false negative results [52,56,59–61]. In our 3D bioprinted models both P-gp and MRP2 were significantly less expressed, highlighting their relevance in the study of these types of substrates. BCRP, another efflux pump localized at the apical side of enterocytes [50] is normally underexpressed on the Caco-2 model [52,53,56,62], thus the lower expression found in the 3D models suggest that they may be less suitable to study the permeability of BCRP substrates. A similar result was obtained in our previous work, where we found a lower expression of BCRP in a 3D model composed by a collagen layer with embedded HIF and Caco-2 + HT29-MTX on top compared to the standard 2D co-culture model [27]. In contrast to all the other transporters, MRP1 (ABCC1) was shown to be more expressed in the 3D bioprinted models compared to the standard 2D model. This efflux pump has been shown to be overexpressed in intestinal stromal myofibroblasts, contributing to the drug resistance of the intestinal stromal compartment critical for regeneration processes [63]. Thus, the stromal compartment present in our 3D bioprinted models may contribute to the expression levels of this transporter, better reproducing the drug resistance mechanisms found *in vivo*. Overall, the expression of transporters in the 3D bioprinted models indicates that

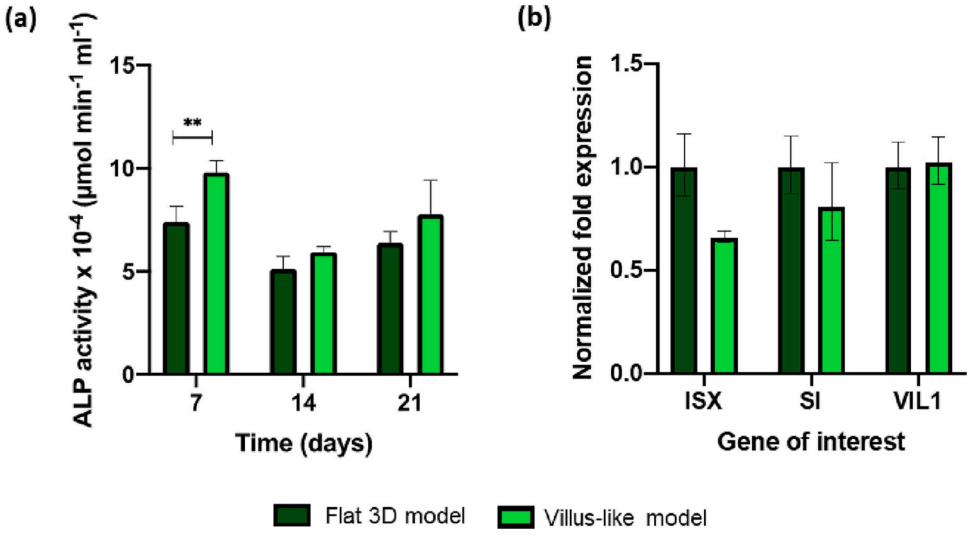

Fig. 5. Quantification of intestinal differentiation markers in the flat and villi bioprinted models of mucosa. (a) ALP activity levels at different timepoints (7, 14 and 21 days) during the culture; and (b) expression of ISX, SI and VIL1 genes after 21 days in culture. For (a) results are the average of triplicates, bars represent the standard error of the mean (SEM) and statistical differences were calculated using 2-way ANOVA multiple comparisons to compare the levels of ALP in the different configurations for each timepoint ($p < 0.01$ is denoted by **). For (b) results are the average of triplicates, bars represent upper and lower limits and statistical differences were calculated using the log transformed data with 2-way ANOVA multiple comparisons to compare expression of each gene between configurations.

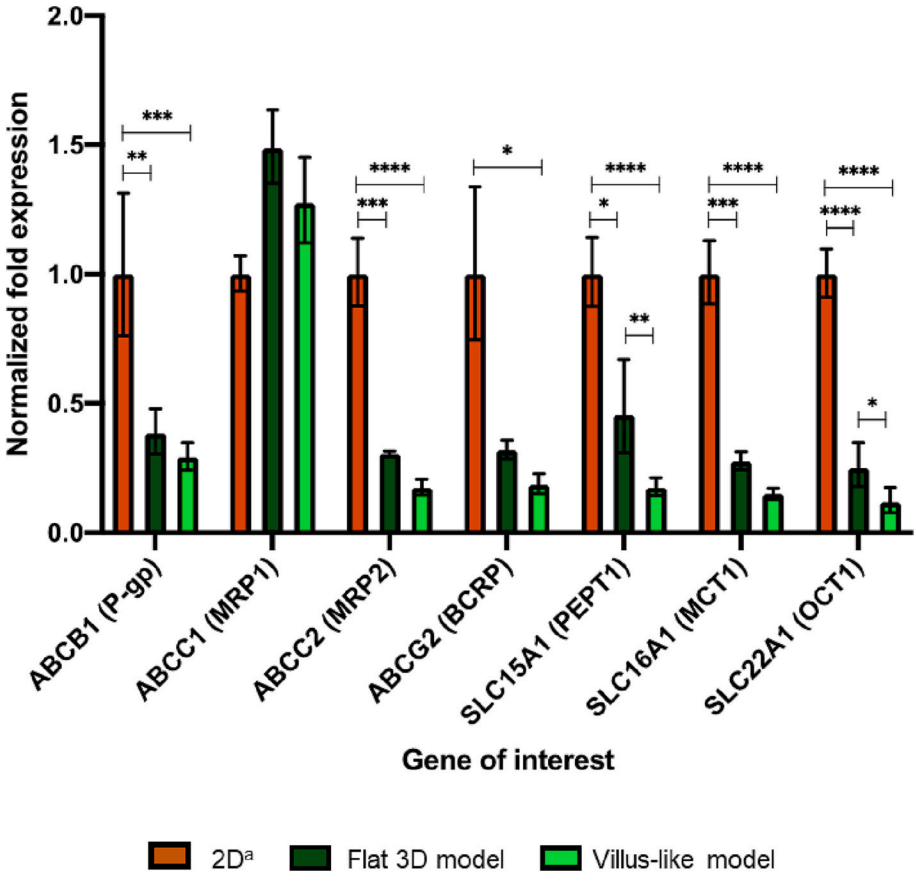

Fig. 6. Normalized genetic expression of different intestinal transporters between the 2D co-culture and the 3D bioprinted models (flat and villi) after 21 days in culture. Results are the average of triplicates, and bars represent the upper and lower limits. Statistical differences were calculated using the log transformed data with 2-way ANOVA multiple comparisons ($p < 0.05$ is denoted by *, $p < 0.01$ is denoted by **, $p < 0.001$ is denoted by *** and $p < 0.0001$ are denoted by ****). ([a]) Data taken from [27].

these models containing both the epithelial and stromal compartments better mimic the carrier-mediated transporters of the small intestine, as compared to standard 2D co-culture models.

3.5. Expression of junction proteins and ECM components in the villi model

We further evaluated the expression of ZO-1, a tight junction protein, β-catenin, involved in cell-cell adhesion and intercellular junctions; and fibronectin and collagen type IV, key components of the ECM in our villus-like bioprinted model of the intestinal mucosa [64].

Two different villus-like structures are depicted in Fig. 7a, b, where it is possible to observe that epithelial cells fully covered the microstructures and strongly expressed β-catenin, E-cadherin and F-actin. Fibronectin signal is also visible, mostly expressed on the tip region. Fig. 7c and d shows detailed images of the epithelial monolayer. Fig. 7c shows the expression of collagen type IV and fibronectin, which are higher under the epithelial layer, suggesting the formation of a basement membrane, as we previously observed [31]. Fig. 7d shows high expression of both β-catenin and ZO-1, and confirms that epithelial cells present the characteristic columnar morphology and polarization expected for intestinal enterocytes. Also, these epithelial cells show different cell heights and shapes along the villi as a response to the highly curved microstructure as we observed previously [26]. We showed that TEER values were within the physiological range for the 3D villi model, which is significantly lower than the standard Caco-2 model. However, cells were still able to form tight junctions and produce an adhesive protein layer, forming a cohesive and differentiated monolayer, which is central for reliable permeability studies.

3.6. P-gp activity

Besides assessing the genetic expression of P-gp, we also assessed its activity. As an efflux pump, P-gp can decrease the permeability of compounds, preventing them from entering the cell by actively pumping them back to the lumen. This transporter is also capable of actively pumping out of the cell compounds that are on the basolateral side [50,66].

To assess P-gp activity in our bioprinted models of mucosa, we performed a permeability assay with Rho 123 in apical-to-basolateral (AP-BL) and basolateral-to-apical (BL-AP) directions [67]. The efflux ratio BL-AP to AP-BL is typically used to understand the influence of transporters in the permeability of compounds. [68] A similar transport in both directions (ratio close to 1) is expected when the permeability of a drug is dominated by passive diffusion. When an efflux transporter is involved in pumping out the compound, the AP-BL transport is reduced, and the ratio is $\gg 1$. In our villi model, the permeability of Rho 123 was almost six-fold higher in the AP-BL direction (Fig. 8a). This difference can be due to the higher surface area of the villi model compared to the flat configuration but also to a decrease in the P-gp activity. When analyzing the results from the BL-AP direction (Fig. 8b), it is clear that the P_{app} value obtained for the villi model was very similar in both directions, meaning that the efflux ratio was close to 1 (Fig. 8c). In the flat model, the transport of Rho 123 was significantly faster in the BL-AP direction, and thus the efflux ratio was four times higher (Fig. 8c). These results suggest a significant reduction in the activity of the P-gp transporter in the 3D villi model, in agreement with the tendency observed in the gene expression data (Fig. 5). This efflux transporter has been shown to be overexpressed in the standard Caco-2 *in vitro* model [52,60,61]. In a previous work, we demonstrated that when epithelial cells were in the presence of a stromal compartment, the gene expression of P-gp, as well as its activity, was lower than in conventional 2D models

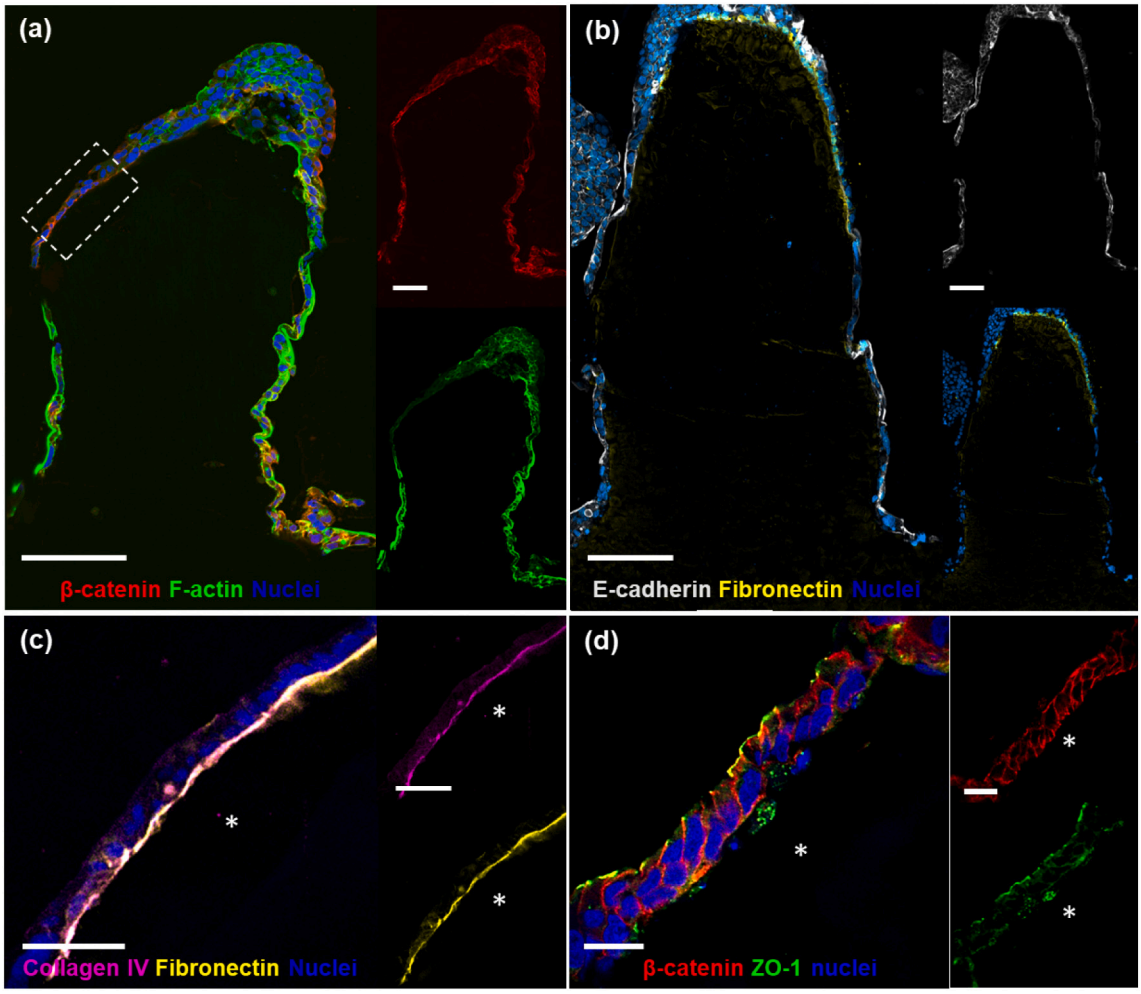

Fig. 7. Protein expression of (a) β-catenin (red), (b) E-cadherin (gray) and fibronectin (yellow), (c) collagen type IV (magenta) and fibronectin (yellow) and (d) β-catenin (red) and ZO-1 (green) in the villi scaffolds after 21 days in culture. * denote the basolateral side of the epithelium (hydrogel). [(a) Scale bar = 100 μm; (b, c) Scale bar = 50 μm].

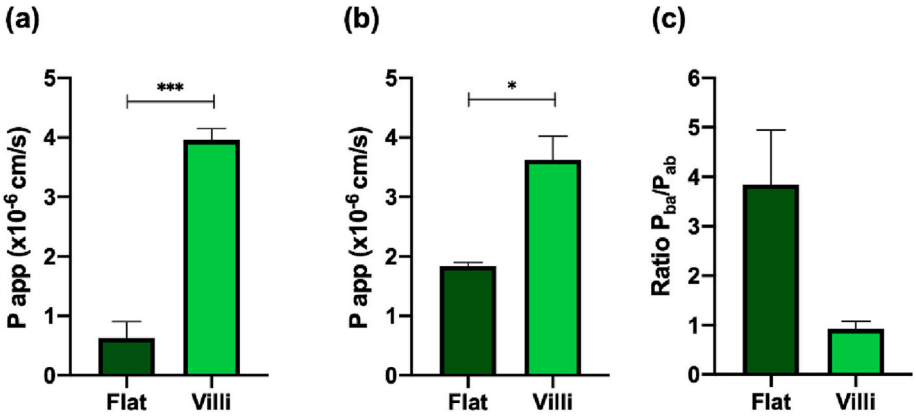

Fig. 8. P_{app} ($\times 10^{-6}$ cm/s) values of Rho 123 in the flat and villi models after 21 days in the (a) apical to basolateral and (b) basolateral to apical directions and (c) ratio of the bidirectional transport. Results are the average of triplicates, and bars represent the standard error of the mean (SEM). Statistical differences were calculated using 2-way ANOVA multiple comparisons to compare P_{app} between each configuration ($p < 0.05$ are denoted by * and $p < 0.001$ are denoted by ***).

[27]. On the other hand, Yi et al. reported that Caco-2 cells growing on villus-like collagen scaffolds expressed significantly less P-gp protein than the conventional Caco-2 model and the authors assumed that the reduced expression resulted from the collagen matrix signaling [69]. In contrast, our results show that this outcome may be attributed to the topography of the epithelial barrier, impacting the expression levels of this efflux transporter. This correlates with the expression gradient of P-gp in the human intestine, being lower in the proximal region, where the surface is covered with intestinal villi, and increasingly expressed in the distal region [70].

Taken together, these results corroborate the hypothesis that cells cultured in a more relevant architecture, akin to *in vivo* intestinal villi, and in presence of a stromal compartment led to a more relevant expression of P-gp, thus increasing the predictive potential of these 3D villi models.

3.7. Permeability

Then, we tested the impact of the improved features observed in our bioprinted model of intestinal mucosa in drug intestinal permeability experiments. For that, we employed three model drugs with different permeability degrees: Metoprolol, Atenolol and Colchicine. Metoprolol is a high permeable compound [fraction absorbed (F_a) > 85 %], crossing the intestinal epithelium by the transcellular route [71,72]. Atenolol, on the other hand, is transported by the paracellular pathway and has moderate permeability (50 % < F_a < 84 %) [73]. Lastly, colchicine has low permeability (F_a < 50 %) and is absorbed by the transcellular route, mainly on the jejunum and ileum. Both P-gp and MPR2 are believed to be involved in the transport of this drug [50,74–78].

Metoprolol showed similar apparent permeability values for both villi and flat bioprinted models (Fig. 9a), suggesting that the transcellular pathway is not affected by the 3D architecture of the model. In the case of atenolol, there was more permeated drug in the 3D villus-like model than in the flat model (Fig. 9b). This can be because the TEER values were significantly lower in the villi model. Since the main transport mechanism of atenolol is through the paracellular route, the

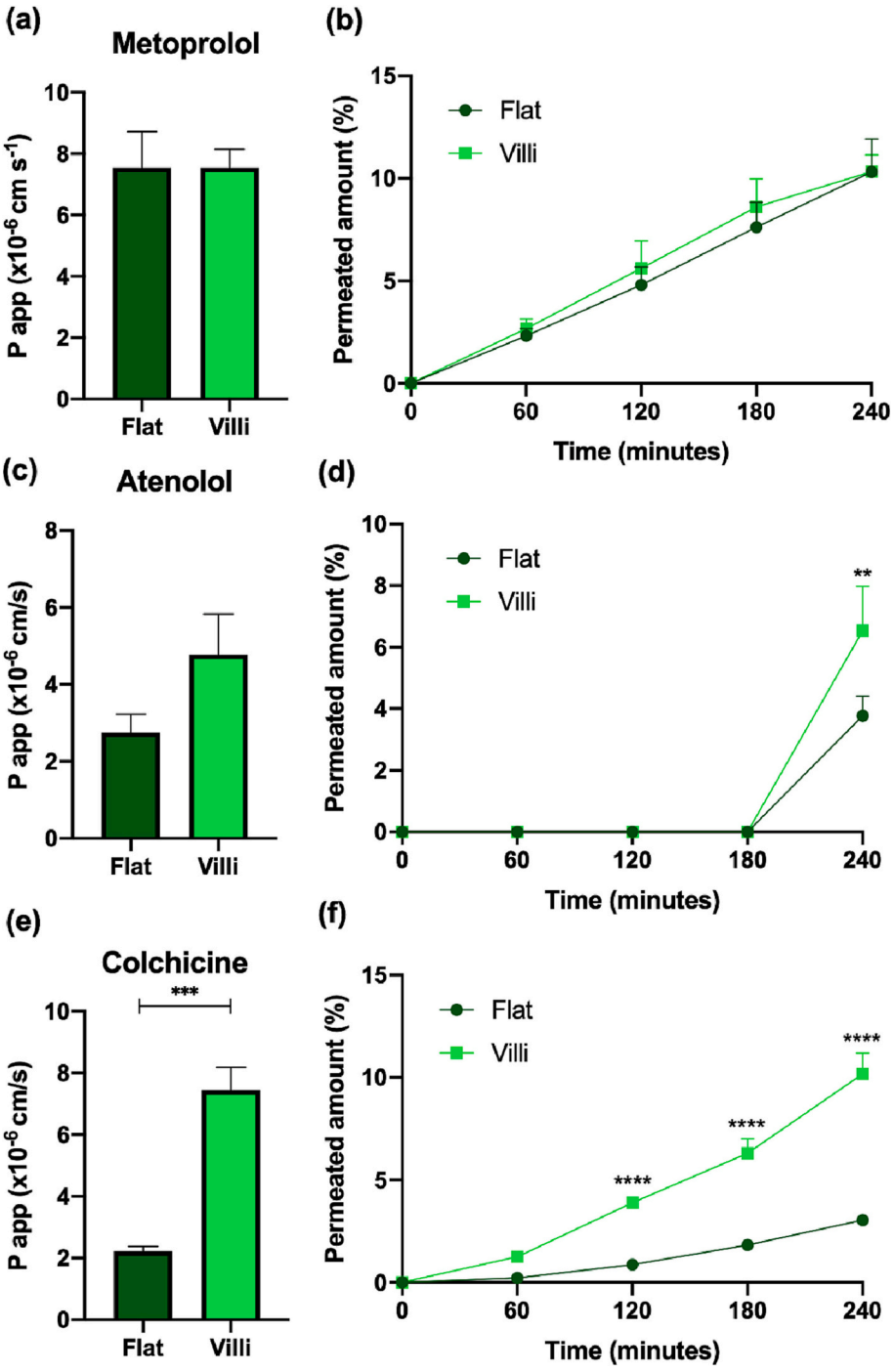

Fig. 9. P_{app} ($\times 10^{-6}$ cm/s) values and percentage of permeated amount of (a, b) metoprolol, (c, d) atenolol and (e, f) colchicine in the flat and villi bioprinted models after 21 days. Results are the average of quadruplicates, and bars represent the standard error of the mean (SEM). Statistical differences were calculated using 2-way ANOVA multiple comparisons to compare P_{app} between each configuration and to compare percentage of permeated amount between each timepoint ($p < 0.01$ is denoted by **, $p < 0.001$ is denoted by *** and $p < 0.0001$ are denoted by ****).

drug would permeate more in a model with looser barrier tightness.

We saw the most significant differences in permeability with Colchicine (Fig. 9c). We found a lower genetic expression of P-gp and MRP2 in the 3D villus-like model, and observed a lower activity of P-gp in this model. This lower activity of the efflux pumps allows colchicine to permeate more than in the flat model. Thus, these permeability results are consistent with the previous results [20,69].

The permeability of paracellular markers in Caco-2 monolayers can be up to 100 times lower when compared to *in vivo* values [79]. Reported values in the literature for the Papp of atenolol in Caco-2 models range from 0.53 to 3.3 $\times$ 10^{-6} cm/s [72,77,80–83], whereas in the rat small intestine is around 11 $\times$ 10^{-6} cm/s [77]. In our villi bioprinted model, atenolol had a permeability of 4.8 $\times$ 10^{-6} cm/s, which is closer to the *in vivo* value. For colchicine, the Papp values reported for the Caco-2 model are around 0.9 $\times$ 10^{-6} cm/s [72,77], and the value is much higher *in vivo* - 25 $\times$ 10^{-6} cm/s [77]. Our villi model presented a Papp of 7.4 $\times$ 10^{-6} cm/s, which relates more to the *in vivo* situation than the Caco-2 model.

These results show that culturing the cells in a more physiological environment, with a stromal compartment and a 3D architecture, leads to better permeability outcomes.

4. Conclusions

In this work, we developed and characterized a novel bioprinted model of the intestinal mucosa. This model comprises both the stromal compartment with human intestinal fibroblasts able to grow, proliferate and express ECM matrix proteins, and the epithelial compartment, where mature enterocytes and goblet cells form a functional epithelial barrier. The model is produced in a robust manner by an affordable bioprinting approach. Furthermore, the fabrication procedure provides samples in a format fully compatible with standard drug permeability assays. By exploiting this feature, we were able to determine that the TEER values of the intestinal mucosa formed are close to what is reported to be found *in vivo*. In addition, we demonstrated that both the presence of a stromal compartment and the presence of a villus-like architecture significantly decreased the expression of most of the studied influx and efflux transporters. We then evaluated the impact of these results on drug permeability assays. We did find that the villi model showed higher permeability values of the paracellular marker atenolol than the flat model, in agreement with the lower TEER values compared to the flat configuration, and more closely resembling the *in vivo* ones. The permeability of colchicine was also more physiologic in the villi configuration, since it was enhanced compared with the flat model, as a consequence of the lower activities of P-gp and MRP2, both involved in the transport of this drug.

In summary, we produced a 3D bioprinted model of the intestinal mucosa with improved physiological features: villus-like architecture and stromal compartment and we showcased the positive influence of considering these two features when evaluating drug permeability.

CRediT authorship contribution statement

Maria Helena Macedo: Conceptualization, Investigation, Methodology, Writing – original draft. **Núria Torras:** Methodology, Visualization, Writing – review & editing. **María García-Díaz:** Writing – review & editing. **Cristina Barrias:** Writing – review & editing. **Bruno Sarmento:** Supervision, Writing – review & editing. **Elena Martínez:** Supervision, Writing – review & editing.

Declaration of competing interest

The authors declare that they have no known competing financial interests or personal relationships that could have appeared to influence the work reported in this paper.

Data availability

Data will be made available on request.

Acknowledgements

This work was financed by Portuguese funds through FCT – Fundação para a Ciência e a Tecnologia/Ministério da Ciência, Tecnologia e Ensino Superior in the framework of the project "Institute for Research and Innovation in Health Sciences" UID/BIM/04293/2019 and by European Union's Horizon 2020 ERC grant agreement No 647863 (COMIET) and ERC-PoC grant agreement No 899906 (GUT3D-PLATE), the CERCA Program/Generalitat de Catalunya (2017-SGR-1079), and the Spanish Ministry of Economy and Competitiveness (TEC2017-83716-C2-1-R). M. H. M. thanks FCT for financial support (SFRH/BD/131587/2017). N. T. thanks the Spanish Ministry of Science and Innovation, Juan de la Cierva program (grant 1040 IJC2019-040289-I).

The results presented here reflect only the views of the authors; the European Commission is not responsible for any use that may be made of the information it contains.

Appendix A. Supplementary data

Supplementary data to this article can be found online at https://doi.org/10.1016/j.bioadv.2023.213564.

References

[1] M.N. Marsh, J.A. Swift, A study of the small intestinal mucosa using the scanning electron microscope, Gut 10 (1969) 940–949.
[2] P. Kelly, I. Menzies, R. Crane, I. Zulu, C. Nickols, R. Feakins, J. Mwansa, V. Mudenda, M. Katubulushi, S. Greenwald, M. Farthing, Responses of small intestinal architecture and function over time to environmental factors in a tropical population, Am. J. Trop. Med. Hyg. 70 (2004) 412–419.
[3] A.G. Castano, M. Garcia-Diaz, N. Torras, G. Altay, J. Comelles, E. Martinez, Dynamic photopolymerization produces complex microstructures on hydrogels in a moldless approach to generate a 3D intestinal tissue model, Biofabrication 11 (2019), 025007.
[4] R. Seeley, T. Stephens, P. Tate, Anatomy and Phisiology, 6 ed., McGraw-Hill, Boston, MA, USA, 2004.
[5] F. Gerbe, E. Sidot, D.J. Smyth, M. Ohmoto, I. Matsumoto, V. Dardalhon, P. Cesses, L. Garnier, M. Pouzolles, B. Brulin, M. Bruschi, Y. Harcus, V.S. Zimmermann, N. Taylor, R.M. Maizels, P. Jay, Intestinal epithelial tuft cells initiate type 2 mucosal immunity to helminth parasites, Nature 529 (2016) 226–230.
[6] N.A. Mabbott, D.S. Donaldson, H. Ohno, I.R. Williams, A. Mahajan, Microfold (M) cells: important immunosurveillance posts in the intestinal epithelium, Mucosal Immunol. 6 (2013) 666–677.
[7] B. Hunyady, E. Mezey, M. Palkovits, Gastrointestinal immunology: cell types in the lamina propria—a morphological review, Acta Physiol. Hung. 87 (2000) 305–328.
[8] D.W. Powell, I.V. Pinchuk, J.I. Saada, X. Chen, R.C. Mifflin, Mesenchymal cells of the intestinal lamina propria, Annu. Rev. Physiol. 73 (2011) 213–237.
[9] M.D. Basson, G. Turowski, N.J. Emenaker, Regulation of human (Caco-2) intestinal epithelial cell differentiation by extracellular matrix proteins, Exp. Cell Res. 225 (1996) 301–305.
[10] A. Vila, N. Torras, A.G. Castano, M. Garcia-Diaz, J. Comelles, T. Perez-Berezo, C. Corregidor, O. Castano, E. Engel, V. Fernandez-Majada, E. Martinez, Hydrogel co-networks of gelatine methacrylate and poly(ethylene glycol) diacrylate sustain 3D functional in vitro models of intestinal mucosa, Biofabrication 12 (2020), 025008.
[11] C. Fritsch, V. Orian-Rousseaul, O. Lefebvre, P. Simon-Assmann, J.M. Reimund, B. Duclos, M. Kedinger, Characterization of human intestinal stromal cell lines: response to cytokines and interactions with epithelial cells, Exp. Cell Res. 248 (1999) 391–406.
[12] F. Pampaloni, E.G. Reynaud, E.H. Stelzer, The third dimension bridges the gap between cell culture and live tissue, Nat. Rev. Mol. Cell Biol. 8 (2007) 839–945.
[13] B.A. Justice, N.A. Badr, R.A. Felder, 3D cell culture opens new dimensions in cell-based assays, Drug Discov. Today 14 (2009) 102–107.
[14] M.J. Bissell, D.C. Radisky, A. Rizki, V.M. Weaver, O.W. Petersen, The organizing principle: microenvironmental influences in the normal and malignant breast, Differentiation 70 (2002) 537–546.
[15] W. Kim, G. Kim, Intestinal villi model with blood capillaries fabricated using collagen-based bioink and dual-cell-printing process, ACS Appl. Mater. Interfaces 10 (2018) 41185–41196.
[16] W. Kim, G.H. Kim, An innovative cell-printed microscale collagen model for mimicking intestinal villus epithelium, Chem. Eng. J. 334 (2018) 2308–2318.

[17] L.R. Madden, T.V. Nguyen, S. Garcia-Mojica, V. Shah, A.V. Le, A. Peier, R. Visconti, E.M. Parker, S.C. Presnell, D.G. Nguyen, K.N. Retting, Bioprinted 3D primary human intestinal tissues model aspects of native physiology and ADME/Tox functions, iScience 2 (2018) 156–167.
[18] J.H. Sung, J. Yu, D. Luo, M.L. Shuler, J.C. March, Microscale 3-D hydrogel scaffold for biomimetic gastrointestinal (GI) tract model, Lab Chip 11 (2011) 389–392.
[19] Y. Wang, D.B. Gunasekara, M.I. Reed, M. DiSalvo, S.J. Bultman, C.E. Sims, S. T. Magness, N.L. Allbritton, A microengineered collagen scaffold for generating a polarized crypt-villus architecture of human small intestinal epithelium, Biomaterials 128 (2017) 44–55.
[20] J. Yu, S. Peng, D. Luo, J.C. March, In vitro 3D human small intestinal villous model for drug permeability determination, Biotechnol. Bioeng. 109 (2012) 2173–2178.
[21] I.J. Hidalgo, T.J. Raub, R.T. Borchardt, Characterization of the human colon carcinoma cell line (Caco-2) as a model system for intestinal epithelial permeability, Gastroenterology 96 (1989) 736–749.
[22] P.V. Balimane, S. Chong, Cell culture-based models for intestinal permeability: a critique, Drug Discov. Today 10 (2005) 335–343.
[23] A. Abbott, Biology's new dimension, Nature 424 (2003) 870–872.
[24] K.R. Johnson, J.L. Leight, V.M. Weaver, Demystifying the effects of a three-dimensional microenvironment in tissue morphogenesis, Methods Cell Biol. 83 (2007) 547–583.
[25] H.J. Kim, H. Li, J.J. Collins, D.E. Ingber, Contributions of microbiome and mechanical deformation to intestinal bacterial overgrowth and inflammation in a human gut-on-a-chip, Proc. Natl. Acad. Sci. 113 (2016) E7–15.
[26] G. Altay, S. Tosi, M. García-Díaz, E. Martínez, Imaging the cell morphological response to 3D topography and curvature in engineered intestinal tissues, Front. Bioeng. Biotechnol. 8 (2020) 294.
[27] M.H. Macedo, A.S. Barros, E. Martínez, C.C. Barrias, B. Sarmento, All layers matter: innovative three-dimensional epithelium-stroma-endothelium intestinal model for reliable permeability outcomes, J. Control. Release 341 (2022) 414–430.
[28] S.H. Kim, M. Chi, B. Yi, S.H. Kim, S. Oh, Y. Kim, S. Park, J.H. Sung, Three-dimensional intestinal villi epithelium enhances protection of human intestinal cells from bacterial infection by inducing mucin expression, Integr. Biol. 6 (2014) 1122–1131.
[29] S.J.P. Callens, R.J.C. Uyttendaele, L.E. Fratila-Apachitei, A.A. Zadpoor, Substrate curvature as a cue to guide spatiotemporal cell and tissue organization, Biomaterials 232 (2020), 119739.
[30] L. Pieuchot, J. Marteau, A. Guignandon, T. Dos Santos, I. Brigaud, P.-F. Chauvy, T. Cloatre, A. Ponche, T. Petithory, P. Rougerie, M. Vassaux, J.-L. Milan, N. Tusamda Wakhloo, A. Spangenberg, M. Bigerelle, K. Anselme, Curvotaxis directs cell migration through cell-scale curvature landscapes, Nat. Commun. 9 (2018) 3995.
[31] N. Torras, J. Zabalo, E. Abril, A. Carré, M. García-Díaz, E. Martínez, A bioprinted 3D gut model with crypt-villus structures to mimic the intestinal epithelial-stromal microenvironment, Biomater. Adv. 153 (2023) 213534.
[32] A.V. Shinde, C. Humeres, N.G. Frangogiannis, The role of α-smooth muscle actin in fibroblast-mediated matrix contraction and remodeling, Biochim. Biophys. Acta (BBA) - Mol. Basis Dis. 1863 (2017) 298–309.
[33] S.A. Hewes, R.L. Wilson, M.K. Estes, N.F. Shroyer, S.E. Blutt, K.J. Grande-Allen, In vitro models of the small intestine: engineering challenges and engineering solutions, Tissue Eng. B Rev. 26 (2020) 313–326.
[34] J.M. Allaire, S.M. Crowley, H.T. Law, S.-Y. Chang, H.-J. Ko, B.A. Vallance, The intestinal epithelium: central coordinator of mucosal immunity, Trends Immunol. 39 (2018) 677–696.
[35] V. De Gregorio, G. Imparato, F. Urciuolo, P.A. Netti, 3D stromal tissue equivalent affects intestinal epithelium morphogenesis in vitro, Biotechnol. Bioeng. 115 (2018) 1062–1075.
[36] R.H. Dosh, A. Essa, N. Jordan-Mahy, C. Sammon, C.L. Le Maitre, Use of hydrogel scaffolds to develop an in vitro 3D culture model of human intestinal epithelium, Acta Biomater. 62 (2017) 128–143.
[37] M.H. Macedo, E. Martinez, C. Barrias, B. Sarmento, Development of an improved 3D in vitro intestinal model to perform permeability studies of paracellular compounds, Front. Bioeng. Biotechnol. 8 (2020) 1076.
[38] J. Pusch, M. Votteler, S. Gohler, J. Engl, M. Hampel, H. Walles, K. Schenke-Layland, The physiological performance of a three-dimensional model that mimics the microenvironment of the small intestine, Biomaterials 32 (2011) 7469–7478.
[39] I. Legen, M. Salobir, J. Kerc, Comparison of different intestinal epithelia as models for absorption enhancement studies, Int. J. Pharm. 291 (2005) 183–188.
[40] J.D. Söderholm, L. Hedman, P. Artursson, L. Franzén, J. Larsson, N. Pantzar, J. Permert, G. Olaison, Integrity and metabolism of human ileal mucosa in vitro in the Ussing chamber, Acta Physiol. Hung. 162 (1998) 47–56.
[41] N. Li, D. Wang, Z. Sui, X. Qi, L. Ji, X. Wang, L. Yang, Development of an improved three-dimensional in vitro intestinal mucosa model for drug absorption evaluation, Tissue Eng. Part C: Methods 19 (2013) 708–719.
[42] D.H. Alpers, A. Mahmood, M. Engle, F. Yamagishi, K. DeSchryver-Kecskemeti, The secretion of intestinal alkaline phosphatase (IAP) from the enterocyte, J. Gastroenterol. 29 (1994) 63–67.
[43] B.F. Hinnebusch, A. Siddique, J.W. Henderson, M.S. Malo, W. Zhang, C.P. Athaide, M.A. Abedrapo, X. Chen, V.W. Yang, R.A. Hodin, Enterocyte differentiation marker intestinal alkaline phosphatase is a target gene of the gut-enriched Kruppel-like factor, Am. J. Physiol. Gastrointest. Liver Physiol. 286 (2004) G23–G30.
[44] T. Sato, D.E. Stange, M. Ferrante, R.G. Vries, J.H. Van Es, S. Van den Brink, W. J. Van Houdt, A. Pronk, J. Van Gorp, P.D. Siersema, H. Clevers, Long-term expansion of epithelial organoids from human colon, adenoma, adenocarcinoma, and Barrett's epithelium, Gastroenterology 141 (2011) 1762–1772.
[45] E. Suh, P.G. Traber, An intestine-specific homeobox gene regulates proliferation and differentiation, Mol. Cell. Biol. 16 (1996) 619–625.
[46] P.G. Traber, L. Yu, G.D. Wu, T.A. Judge, Sucrase-isomaltase gene expression along crypt-villus axis of human small intestine is regulated at level of mRNA abundance, Am. J. Phys. 262 (1992) G123–G130.
[47] E. Friederich, K. Vancompernolle, D. Louvard, J. Vandekerckhove, Villin function in the organization of the actin cytoskeleton. Correlation of in vivo effects to its biochemical activities in vitro, J. Biol. Chem. 274 (1999) 26751–26760.
[48] G.P. Lobo, S. Hessel, A. Eichinger, N. Noy, A.R. Moise, A. Wyss, K. Palczewski, J. von Lintig, ISX is a retinoic acid-sensitive gatekeeper that controls intestinal beta,beta-carotene absorption and vitamin A production, FASEB J. 24 (2010) 1656–1666.
[49] B. Gericke, M. Amiri, H.Y. Naim, The multiple roles of sucrase-isomaltase in the intestinal physiology, Mol. Cell. Pediatr. 3 (2016) 2.
[50] M. Estudante, J.G. Morais, G. Soveral, L.Z. Benet, Intestinal drug transporters: an overview, Adv. Drug Deliv. Rev. 65 (2013) 1340–1356.
[51] Z. Liu, K. Liu, The transporters of intestinal tract and techniques applied to evaluate interactions between drugs and transporters, Asian J. Pharm. Sci. 8 (2013) 151–158.
[52] S. Brück, J. Strohmeier, D. Busch, M. Drozdzik, S. Oswald, Caco-2 cells - expression, regulation and function of drug transporters compared with human jejunal tissue, Biopharm. Drug Dispos. 38 (2017) 115–126.
[53] C. Hilgendorf, G. Ahlin, A. Seithel, P. Artursson, A.L. Ungell, J. Karlsson, Expression of thirty-six drug transporter genes in human intestine, liver, kidney, and organotypic cell lines, Drug Metab. Dispos. 35 (2007) 1333–1340.
[54] D. Herrera-Ruiz, Q. Wang, O.S. Gudmundsson, T.J. Cook, R.L. Smith, T.N. Faria, G. T. Knipp, Spatial Expression Patterns of Peptide Transporters in the Human and Rat Gastrointestinal Tracts, Caco-2 In Vitro Cell Culture Model, and Multiple Human Tissues 3, American Association of Pharmaceutical Scientists, 2001, p. E9.
[55] I. Behrens, W. Kamm, A.H. Dantzig, T. Kissel, Variation of peptide transporter (PepT1 and HPT1) expression in Caco-2 cells as a function of cell origin, J. Pharm. Sci. 93 (2004) 1743–1754.
[56] N. Maubon, M. Le Vee, L. Fossati, M. Audry, E. Le Ferrec, S. Bolze, O. Fardel, Analysis of drug transporter expression in human intestinal Caco-2 cells by real-time PCR, Fundam. Clin. Pharmacol. 21 (2007) 659–663.
[57] Y. Shu, Research progress in the organic cation transporters, Zhong Nan Da Xue Xue Bao Yi Xue Ban 36 (2011) 913–926.
[58] L.M. Chan, S. Lowes, B.H. Hirst, The ABCs of drug transport in intestine and liver: efflux proteins limiting drug absorption and bioavailability, Eur. J. Pharm. Sci. 21 (2004) 25–51.
[59] A. Beduneau, C. Tempesta, S. Fimbel, Y. Pellequer, V. Jannin, F. Demarne, A. Lamprecht, A tunable Caco-2/HT29-MTX co-culture model mimicking variable permeabilities of the human intestine obtained by an original seeding procedure, Eur. J. Pharm. Biopharm. 87 (2014) 290–298.
[60] H. Bohets, P. Annaert, G. Mannens, L. Van Beijsterveldt, K. Anciaux, P. Verboven, W. Meuldermans, K. Lavrijsen, Strategies for absorption screening in drug discovery and development, Curr. Top. Med. Chem. 1 (2001) 367–383.
[61] C. Hilgendorf, H. Spahn-Langguth, C.G. Regårdh, E. Lipka, G.L. Amidon, P. Langguth, Caco-2 versus Caco-2/HT29-MTX co-cultured cell lines: permeabilities via diffusion, inside- and outside-directed carrier-mediated transport, J. Pharm. Sci. 89 (2000) 63–75.
[62] J. Taipalensuu, H. Törnblom, G. Lindberg, C. Einarsson, F. Sjöqvist, H. Melhus, P. Garberg, B. Sjöström, B. Lundgren, P. Artursson, Correlation of gene expression of ten drug efflux proteins of the ATP-binding cassette transporter family in normal human jejunum and in human intestinal epithelial Caco-2 cell monolayers, J. Pharmacol. Exp. Ther. 299 (2001) 164–170.
[63] Y.C. Chee, J. Pahnke, R. Bunte, V.A. Adsool, B. Madan, D.M. Virshup, Intrinsic xenobiotic resistance of the intestinal stem cell niche, Dev. Cell 46 (2018) 681–695 e685.
[64] S.Z. Bathaie, N. Faridi, A. Nasimian, H. Heidarzadeh, F. Tamanoi, Chapter one - how phytochemicals prevent chemical carcinogens and/or suppress tumor growth? in: S.Z. Bathaie, F. Tamanoi (Eds.), The Enzymes Academic Press, 2015, pp. 1–42.
[66] J.R. Kunta, P.J. Sinko, Intestinal drug transporters: in vivo function and clinical importance, Curr. Drug Metab. 5 (2004) 109–124.
[67] Y. Wang, D. Hao, W.D. Stein, L. Yang, A kinetic study of Rhodamine123 pumping by P-glycoprotein, Biochim. Biophys. Acta 1758 (2006) 1671–1676.
[68] C.H.M. Versantvoort, R.C.A. Ondrewater, E. Duizer, J.J.M. Van de Sandt, A. J. Gilde, J.P. Groten, Monolayers of IEC-18 cells as an in vitro model for screening the passive transcellular and paracellular transport across the intestinal barrier: comparison of active and passive transport with the human colon carcinoma Caco-2 cell line, Environ. Toxicol. Pharmacol. 11 (2002) 335–344.
[69] B. Yi, K.Y. Shim, S.K. Ha, J. Han, H.-H. Hoang, I. Choi, S. Park, J.H. Sung, Three-dimensional in vitro gut model on a villi-shaped collagen scaffold, BioChip J. 11 (2017) 219–231.
[70] S. Mouly, M.F. Paine, P-glycoprotein increases from proximal to distal regions of human small intestine, Pharm. Res. 20 (2003) 1595–1599.
[71] I. Lozoya-Agullo, M. Zur, A. Beig, N. Fine, Y. Cohen, M. Gonzalez-Alvarez, M. Merino-Sanjuan, I. Gonzalez-Alvarez, M. Bermejo, A. Dahan, Segmental-dependent permeability throughout the small intestine following oral drug administration: single-pass vs. Doluisio approach to in-situ rat perfusion, Int. J. Pharm. 515 (2016) 201–208.
[72] I. Lozoya-Agullo, M. Zur, N. Fine-Shamir, M. Markovic, Y. Cohen, D. Porat, I. Gonzalez-Alvarez, M. Gonzalez-Alvarez, M. Merino-Sanjuan, M. Bermejo, A. Dahan, Investigating drug absorption from the colon: single-pass vs. Doluisio approaches to in-situ rat large-intestinal perfusion, Int. J. Pharm. 527 (2017) 135–141.

[73] R.L. DiMarco, D.R. Hunt, R.E. Dewi, S.C. Heilshorn, Improvement of paracellular transport in the Caco-2 drug screening model using protein-engineered substrates, Biomaterials 129 (2017) 152–162.
[74] E. Ben-Chetrit, Colchicine, in: Textbook of Autoinflammation, 2018, pp. 729–749.
[75] A. Dahan, G.L. Amidon, Grapefruit juice and its constituents augment colchicine intestinal absorption: potential hazardous interaction and the role of p-glycoprotein, Pharm. Res. 26 (2009) 883–892.
[76] A. Dahan, H. Sabit, G.L. Amidon, Multiple efflux pumps are involved in the transepithelial transport of colchicine: combined effect of P-glycoprotein and multidrug resistance-associated protein 2 leads to decreased intestinal absorption throughout the entire small intestine, Drug Metab. Dispos. 37 (2009) 2028–2036.
[77] I. Lozoya-Agullo, I. Gonzalez-Alvarez, M. Gonzalez-Alvarez, M. Merino-Sanjuan, M. Bermejo, In situ perfusion model in rat Colon for drug absorption studies: comparison with small intestine and Caco-2 cell model, J. Pharm. Sci. 104 (2015) 3136–3145.
[78] M.L. Ruiz, S.S. Villanueva, M.G. Luquita, J.M. Pellegrino, J.P. Rigalli, A. Arias, E. J. Sanchez Pozzi, A.D. Mottino, V.A. Catania, Induction of intestinal multidrug resistance-associated protein 2 (Mrp2) by spironolactone in rats, Eur. J. Pharmacol. 623 (2009) 103–106.
[79] P. Artursson, A.L. Ungell, J.E. Lofroth, Selective paracellular permeability in two models of intestinal absorption: cultured monolayers of human intestinal epithelial cells and rat intestinal segments, Pharm. Res. 10 (1993) 1123–1129.
[80] J.D. Irvine, L. Takahashi, K. Lockhart, J. Cheong, J.W. Tolan, H.E. Selick, J. R. Grove, MDCK (Madin-Darby canine kidney) cells: a tool for membrane permeability screening, J. Pharm. Sci. 88 (1999) 28–33.
[81] C. Li, T. Liu, X. Cui, A.S. Uss, K.C. Cheng, Development of in vitro pharmacokinetic screens using Caco-2, human hepatocyte, and Caco-2/human hepatocyte hybrid systems for the prediction of oral bioavailability in humans, J. Biomol. Screen. 12 (2007) 1084–1091.
[82] M. Yazdanian, S.L. Glynn, J.L. Wright, A. Hawi, Correlating partitioning and caco-2 cell permeability of structurally diverse small molecular weight compounds, Pharm. Res. 15 (1998) 1490–1494.
[83] Y. Yang, P.J. Faustino, D.A. Volpe, C.D. Ellison, R.C. Lyon, L.X. Yu, Biopharmaceutics classification of selected beta-blockers: solubility and permeability class membership, Mol. Pharm. 4 (2007) 608–614.